The Astrophysical Journal, 889:143 (17pp), 2020 February 1 https://doi.org/10.3847/1538-4357/ab64e5
© 2020. The American Astronomical Society. All rights reserved.

Statistical Results for Solar Energetic Electron Spectra Observed over 12 yr with *STEREO*/SEPT

Nina Dresing[1], Frederic Effenberger[2,3], Raúl Gómez-Herrero[4], Bernd Heber[1], Andreas Klassen[1], Alexander Kollhoff[1], Ian Richardson[5,6], and Solveig Theesen[1]

[1] Institut fuer Experimentelle und Angewandte Physik, University of Kiel, Germany; dresing@physik.uni-kiel.de
[2] Helmholtz Centre Potsdam, GFZ German Research Centre for Geosciences, Telegrafenberg, Potsdam, D-14473, Germany
[3] Bay Area Environmental Research Institute, NASA Research Park, Moffett Field, CA 94043, USA
[4] Space Research Group, Universidad de Alcalá, Spain
[5] GPHI and Department of Astronomy, University of Maryland, College Park, MD 20742, USA
[6] Heliospheric Physics Division, NASA Goddard Space Flight Center, Greenbelt, MD 20771, USA
Received 2019 September 5; revised 2019 November 29; accepted 2019 December 20; published 2020 February 3

Abstract

This work presents a statistical analysis of near-relativistic solar energetic electron event spectra near 1 au. We use measurements of the Solar Electron and Proton Telescope (SEPT) on board *STEREO* in the energy range of 45–425 keV and utilize the SEPT electron event list containing all electron events observed by *STEREO A* and *STEREO B* from 2007 through 2018. We select 781 events with significant signal-to-noise ratios for our analysis and fit the spectra with single or broken-power-law functions of energy. We find 437 events showing broken power laws and 344 events only showing a single power law in the energy range of SEPT. For those events with broken power laws, we find a mean break energy of about 120 keV. We analyze the dependence of the spectral index on the rise times and peak intensities of the events as well as on the presence of relativistic electrons. The results show a relation between the power law spectral index and the rise times of the events with softer spectra belonging to rather impulsive events. Long rise-time events are associated with hard spectra as well as with the presence of higher-energy (>0.7 MeV) electrons. This group of events cannot be explained by a pure flare scenario but suggests an additional acceleration mechanism, involving a prolonged acceleration and/or injection of the particles. A dependence of the spectral index on the longitudinal separation from the parent solar source region was not found. A statistical analysis of the spectral indices during impulsively rising events where the rise times are below 20 minutes is also shown.

Unified Astronomy Thesaurus concepts: Heliosphere (711); Interplanetary particle acceleration (826); Solar flares (1496); Spectral index (1553); Solar energetic particles (1491); Radio bursts (1339); Solar coronal mass ejection shocks (1997)

1. Introduction

While magnetic reconnection in solar flares is generally regarded as the mechanism that accelerates solar energetic electrons up to relativistic energies (e.g., Mann 2015), the role of other acceleration mechanisms such as coronal mass ejection (CME)–driven shocks is still under debate. On the one hand, the existence of type II radio bursts demonstrates that CME-driven shocks do accelerate electrons of a few keV (Holman & Pesses 1983). On the other hand, interplanetary (IP) shocks at 1 au appear to be largely ineffective in accelerating near-relativistic (NR) electrons, i.e., with energies of several tens to several hundreds of keVs (Tsurutani & Lin 1985; Dresing et al. 2016; Yang et al. 2019). Other cases of shock-accelerated electrons, e.g., at Earth's bow shock (Anderson et al. 1979), the heliospheric termination shock (Decker et al. 2005), or at corotating interaction regions (Simnett et al. 2005) usually show only electrons up to around 100 keV. Furthermore, model results of electron-shock acceleration (e.g., Guo & Giacalone 2015; Trotta & Burgess 2019) show that energies of above 100 keV can only be produced under certain conditions and by high-Mach-number shocks, which is supported by observations of MeV electrons apparently accelerated at Saturn's (high-Mach-number) bow shock (Masters et al. 2013) where a main ingredient seems to be the presence of large-amplitude magnetic fluctuations. Favorable conditions for efficient electron acceleration at CME-driven shocks might form at certain distances and positions along the shock front. However, the presence of widespread electron events (Dresing et al. 2014), especially those which show prompt electron onsets and significant anisotropies over wide longitudinal ranges (e.g., Gómez-Herrero et al. 2015; Lario et al. 2016; Dresing et al. 2018), is not only hard to explain by a sole flare acceleration scenario but also (based on the above facts) by acceleration at a coronal or CME-driven shock. During such widespread events, it is also not clear if the accelerator itself is extended or whether the IP injection process, i.e., the particle release into IP space, is responsible for the wide particle spread in these events. Therefore, mechanisms like the spreading of magnetic field lines close to the Sun (Klein et al. 2008), enhanced perpendicular transport, e.g., through field line meandering (Laitinen et al. 2016) or particle scattering at magnetic irregularities (Dröge 2003), may play an important role as well. The presence of large-scale particle traps (Dresing et al. 2018), possibly caused by interacting CMEs, may be a further mechanism not only able to explain wide particle injections but also efficient electron acceleration. Dresing et al. (2018) suggested that the presence of a large-scale particle trap may have provided the conditions for efficient electron acceleration during the 2013 December 26 widespread SEP event, which was also characterized by an extraordinarily long-lasting electron injection, supposedly caused by continuous leakage from the trap.

In a statistical study of 31 impulsive electron events observed with *Wind*/3DP (Lin et al. 1995), Krucker et al. (2007) compared the spectral index δ of the in situ observed electrons with that of the hard X-ray (HXR) photon spectrum of the corresponding flare. For a group of prompt events, they find a clear correlation of about unity, suggesting that both the X-ray-emitting electrons and the in situ electrons belong to the same source population. However, a second group of delayed events shows harder in situ electron spectra and a much weaker correlation with the X-ray spectrum, suggesting that the source spectrum may have been altered after the flare acceleration. This could be caused, for example, by ongoing acceleration in postflare loops (Klein et al. 2005) or by reacceleration in the CME-shock environment (Petrosian 2016). Indeed, the common delays between the onset of IP electron events and the solar injection time, inferred from the associated flare observation, as well as ramp-like, i.e., gradual, rising phases during well-connected electron events, were attributed to CME-driven shocks (Haggerty & Roelof 2002, 2009). Oka et al. (2018) summarized in their review on NR electron spectra that reconnection processes, like solar flares or Earth's magnetotail reconnection, will instead produce softer spectra with spectral indices $\delta \sim$ 3–5 while shocks are known to produce harder spectra of $\delta \sim$ 2–4.

A solar energetic particle (SEP) spectrum observed in situ in the IP medium may also have been altered by various transport effects. The generation of Langmuir waves by electrons of a few to tens of keV, for example, may cause energy loss and the formation of a spectral break. Model results by Kontar & Reid (2009) yield a break energy of 35 keV, due to the spectral hardening of the lower-energy component, whereas above the break, the spectrum resembles the unchanged injection spectrum.

Another transport effect may arise due to the energy-dependent diffusion coefficient describing the scattering of energetic particles at magnetic irregularities. Energy-dependent transport modeling applied to different SEP events (Dröge 2000; Agueda et al. 2014) shows that the mean free path of NR electrons decreases with increasing energy. This means that the higher-energy electrons experience stronger scattering than the lower-energy ones, with a constant mean free path for electrons above ~1 GV (~1600 keV).

While the above transport effects may lead to a spectral break in the NR electron spectrum, as is frequently observed during impulsive electron events (e.g., Lin et al. 1982; Reames et al. 1985; Krucker et al. 2009), such a break could also be caused by the acceleration process. In particular, a typical feature of shock acceleration is a break or a rollover corresponding to the acceleration limit caused by the finite extent of the shock front and/or the acceleration time (Ellison & Ramaty 1985). However, the HXR spectrum of a solar flare can also show a broken-power-law shape with a break energy of about 100 keV as reported by Dulk et al. (1992).

In this work, we analyze the spectra of NR electron events observed by the two *STEREO* spacecraft (Kaiser et al. 2007) from 2007 until end of 2018. We do not separate or discard events depending on their rise times, intensities, delays, or correlations to solar flares, CMEs, or type III or type II radio bursts. To determine the spectra, we use data of the Solar Electron and Proton Telescope (SEPT; Müller-Mellin et al. 2008) with additional contributions from the High Energy Telescope (HET; von Rosenvinge et al. 2008).

2. Event Selection and Data Analysis

Our study is based on the electron event list[7] of SEPT on board the two *STEREO* spacecraft. SEPT measures electrons from 45 to 425 keV in 15 energy channels and in four viewing directions. The list is based on observations of 55–85 keV electrons usually from the Sun telescope, which looks along the nominal *Parker* spiral toward the Sun. However, if another of the four telescopes observes an earlier onset time, we use observations from this one.

For each event, the list provides the onset time, defined by the time when the intensity shows a 3σ increase above the pre-event background. If the statistics allow, the original 1 minute data is used, otherwise longer averages are applied. These averaging windows are taken as an estimate for the onset uncertainty and are also listed. Furthermore, the list provides the peak times and peak intensities, which are determined with at least 10 minute averages or with the same averaging as used for the onset times, if longer averaging is applied. The peak time and intensity may be missing if another event, following shortly after, masks the event maximum. A comment is provided and the events are numbered.

The list starts at the beginning of the *STEREO* science mission in 2007 January and events up to the end of 2018 are taken into account for the present study. Due to the loss of contact with *STEREO B*, there are no *STEREO B* events after 2014 September. The total number of events is 925: 557 at *STEREO A* and 368 at *STEREO B*. For the present analysis, all events of the list are taken into account regardless of the impulsiveness of the time profiles (defined by the rise time of the events), possible delays with respect to their solar counterpart, or the presence of radio type II and type III bursts, or CMEs.

For each of the listed events, we determine the maximum intensity spectrum, taking the peak intensity of each energy channel based on 10 minutes averaged data. We subtract the pre-event background for each energy channel, which includes background caused by preceding events, and use the telescope which observes the highest peak intensity. If no difference between the four viewing directions is observed, the Sun telescope is used. Energy channels are excluded from the spectrum if their peak intensity does not increase significantly (3σ) above its pre-event background. We also exclude higher-energy bins if the two neighboring lower bins were already excluded because of the significance level. Furthermore, we exclude energy bins if they show higher intensities than their lower-energy neighbor, which would correspond to a power law with a positive slope. This is not expected for peak intensity spectra of solar energetic electron events and might be caused by another electron population mixing with the analyzed event or by instrumental effects. Finally, if the real peak of an event is masked by the onset of another, more intense, event, we use the intensities detected directly before the new increase. If the final spectrum contains fewer than four points (which implies a maximum energy of 80 keV) or the fit results is unreliable based on very high reduced chi-square values, the event is excluded from our analysis. After applying the above restrictions, 781 events are left, which are used in a statistical analysis.

We use the scipy.odr package of Python to fit the data including uncertainties in intensity and energy, where the width

[7] http://www2.physik.uni-kiel.de/stereo/downloads/sept_electron_events.pdf

of the energy bins serves as the uncertainty. To characterize each spectrum, we first assume a broken-power-law shape,

$$\frac{dJ}{dE} \propto \begin{cases} E^{\delta_1} & E < E_b \\ E^{\delta_2} & E > E_b \end{cases}, \quad (1)$$

where δ_1 (δ_2) denotes the spectral index below (above) the break energy E_b. The fitting procedure is as follows: for a set of assumed break-point positions, we fit two single power-law functions to each part of the data set separated by the assumed break point. This set of assumed break points is determined by the energy binning of SEPT and the restriction that at least three energy bins have to lie on each side of the assumed break point. After performing fits for the whole set of potential break points, the fit yielding the smallest difference between resulting and assumed break point is chosen to be the best. The break energy is determined by the intersection of the two single power-law fits. Afterwards, we also fit a single power law to the whole spectrum and chose the best of the two (single or broken power law) based on their reduced chi squares. The SEPT energy range (45–425 keV) together with our fitting procedure limits the positions of break points, which can be determined, to the energy range between ~70 and ~300 keV.

Due to its measurement principle (the magnet-foil technique), SEPT's electron measurements can be subject to ion contamination (Wraase et al. 2018): the electron telescopes are covered by a thin (4.95 μm) Parylene foil, which leaves the electron spectrum essentially unchanged but stops ions of energies up to ~400 keV. Ions with energies above this limit can cross the foil and stop inside the top silicon detector, being registered as electrons by the sensor. This effect, mainly caused by protons of a few hundred keV but below 1 MeV, is well known and can be identified as described in the instrument caveats.[8] A further potential contamination effect caused by electrons and protons in the MeV range, which are able to enter the telescope from the side. This is not identified so straightforwardly in the data but can be corrected by using simulated response functions of the telescope (see Kollhoff et al. 2018; Wraase et al. 2018). We apply a contamination correction to the level2-electron data consisting of three parts: (i) protons in the hundreds of keV range, determined by the SEPT proton measurements, (ii) relativistic electrons, determined using the measured spectra of the HET electrons from 0.7–4 MeV, and (iii) high-energy protons, determined by HET proton measurements from 13 to 100 MeV. The input spectra for this correction were determined by using the measured spectra of the respective particles in the same time window used to determine the peak intensity spectrum at SEPT. Because of the upper energy limit of the HET measurements, the input spectra for the correction were extrapolated to 10 MeV for electrons and 1 GeV for protons assuming a single power-law shape. Furthermore, the electron input spectrum was multiplied by an intercalibration factor of 14 as found by Richardson et al. (2014), comparing the HET with *Solar and Heliospheric Observatory* (*SOHO*)/EPHIN electron intensities. Finally, the contamination correction is also used to exclude SEPT energy bins from the spectrum if the contamination is larger than 50%. For energy bins suffering a smaller but nonzero contamination, we propagate the error of the contaminating intensities to the corrected intensities. Our list of electron events was also synchronized with the >25 MeV proton event list by Richardson et al. (2014) and a nonpublished extended version of that list until 2017 April.

[8] http://www2.physik.uni-kiel.de/stereo/data/sept/level2/SEPT_L2_description.pdf

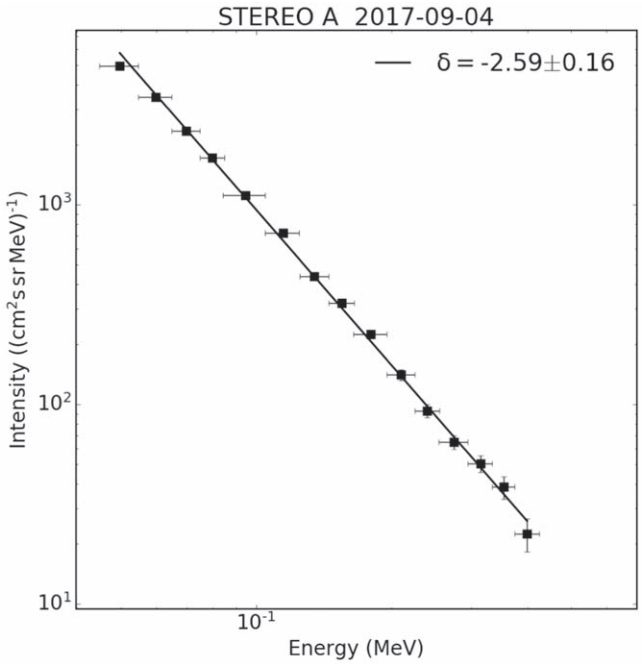

Figure 1. Example of an event with a single power-law peak spectrum.

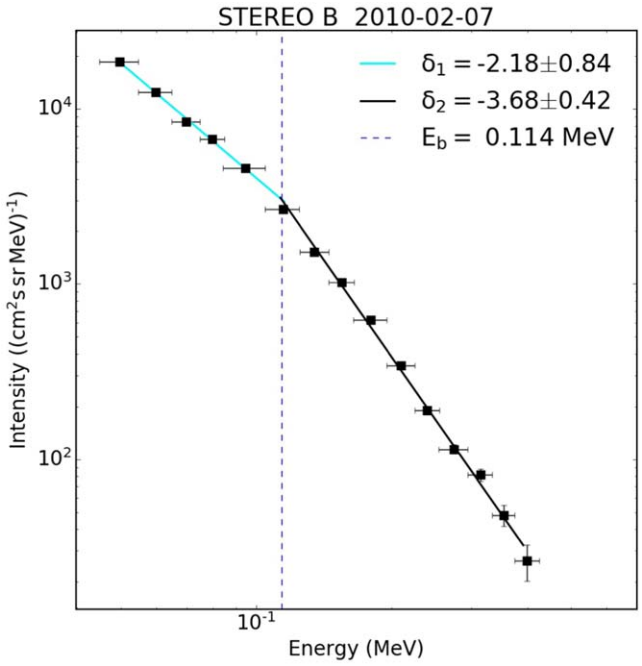

Figure 2. Example of an event with a broken-power-law peak spectrum.

3. Results

3.1. Statistical Results

The analysis of the whole sample of electron events reveals different spectral shapes. While some events (344) show a single power-law shape like the one shown in Figure 1, others (437) are described by a broken power law (see Figure 2),

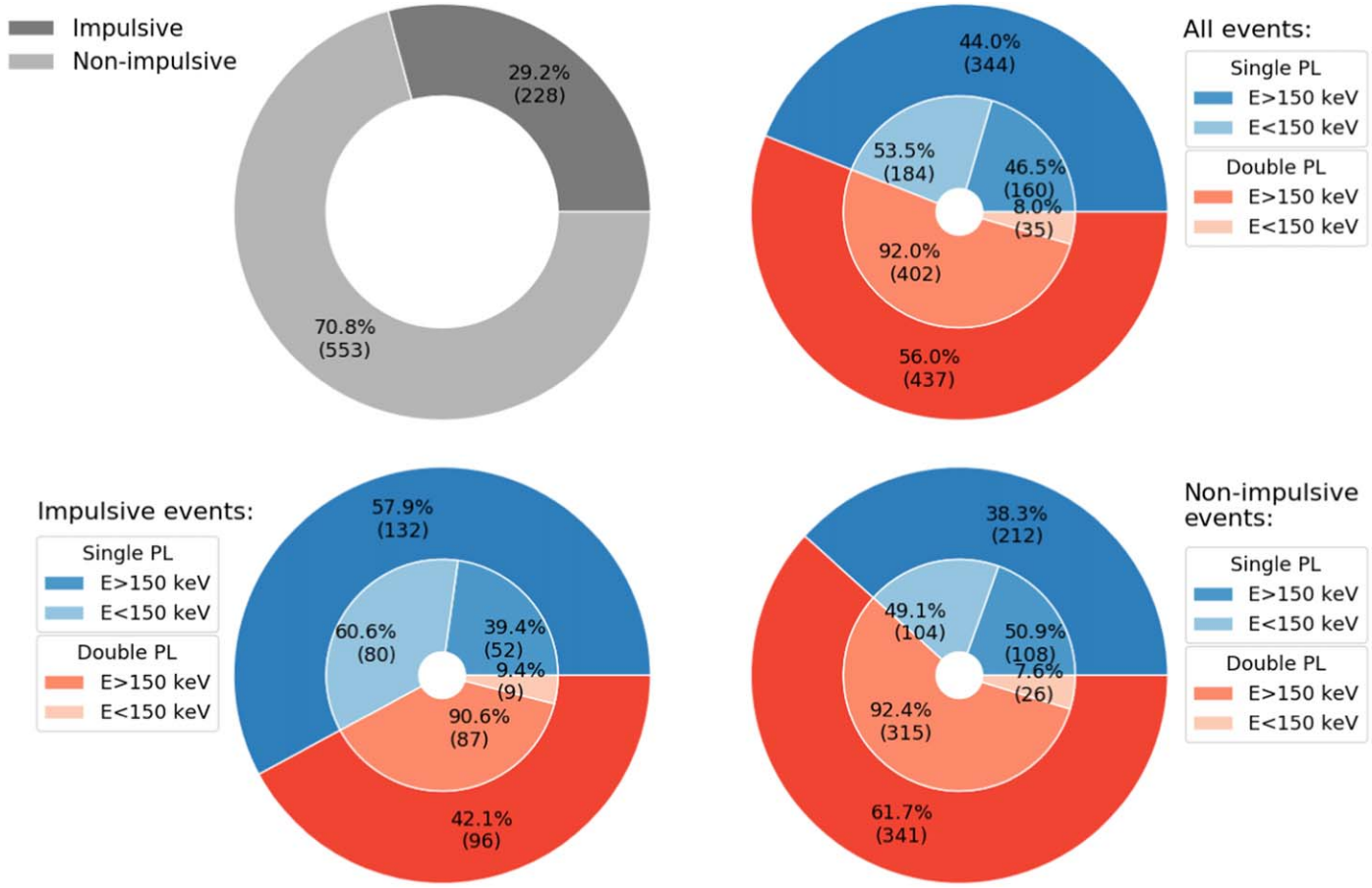

Figure 3. Statistical results for electron event properties. Top left: relative numbers of events with impulsive (<20 minutes) and nonimpulsive rise times. Top right: the outer ring shows the relative numbers of events with single power shape (blue) and broken-power-law shapes (red). The inner ring further separates the events into subcategories of events detected up to a maximum energy above or below 150 keV (lighter colors belong to the corresponding darker color of the outer ring). The bottom panels are in the same format as the top-right panel, but show results for the subsamples of impulsive (left) and nonimpulsive (right) events.

which is the typical shape previously reported in the analyzed energy range especially for impulsive solar energetic electron events (e.g., Krucker et al. 2009). As a subsample of all of the SEPT electron events, we select those events with impulsive rise times, which we define as showing delays between onset and peak time smaller than 20 minutes in the energy range of 55–85 keV. This criterion is based on the distribution of rise times discussed below in relation to Figure 11. Note that we use the term "impulsive" here only with regard to the time profiles and it does not imply that the event has the characteristics (such as ion compositional signatures) of an "impulsive" solar particle event (e.g., Reames 1999). Figure 3 (top left) shows that 29% of the events were impulsive, while the majority were nonimpulsive with rise times >20 minutes. The top-right diagram of Figure 3 shows, in the outer ring, that the event spectra were nearly evenly divided between single power laws (blue; 44%) and broken power laws (red; 56%). The outer rings of the bottom left and right panels of Figure 3 similarly summarize the fractions of single and broken-power-law spectra for impulsive and nonimpulsive events. The inner rings in Figure 3 represent the relative numbers of events with maximum energies above or below 150 keV. The maximum energy is the mean energy of the highest-energy bin used in the fit and is usually determined by the highest-energy bin showing a 3σ increase above its pre-event background. However, if energy bins are excluded because of proton or high-energy electron contamination, the maximum energy may be underestimated. The top-right and bottom diagrams show that out of the single power-law events (blue), $\gtrsim$50% have maximum energies <150 keV, implying that a break point at energies $\gtrsim$100 keV would have been missed. Regarding the single power-law events reaching higher energies, one possibility is that a break point was present but detection was still limited by the observations and the fitting procedure, which requires at least three points on each side of the break. In this case, the break could have been below 70 keV or above 300 keV. Alternatively, the spectrum could in fact have been a single power law.

Figure 4 shows histograms of the spectral indices (left) and the break energy (right) for events showing a double power-law shape. The mean spectral index below (above) the break is $\delta_1 = -2.53 \pm 0.87$ ($\delta_2 = -3.93 \pm 1.53$) with the distribution of δ_2 being wider. Note that the uncertainties provided above represent the widths of the distributions determined by the span between the first and third quartiles of the distributions. Because of the non-Gaussian shapes of several of the distributions, we prefer not to use a 1σ uncertainty as provided by Krucker et al. (2009) for their mean spectral indices, which yield smaller values. The mean spectral index for the events showing only a single power law lies between δ_1 and δ_2 with $\delta = -3.47 \pm 1.15$ (not shown). For comparison, Krucker et al. (2009) found values of $\delta_1 = -1.9$, $\delta_2 = -3.6$ for a sample of 62 impulsive electron events observed in solar cycle 23. While the values for δ_2 agree reasonably well, Krucker et al. (2009)

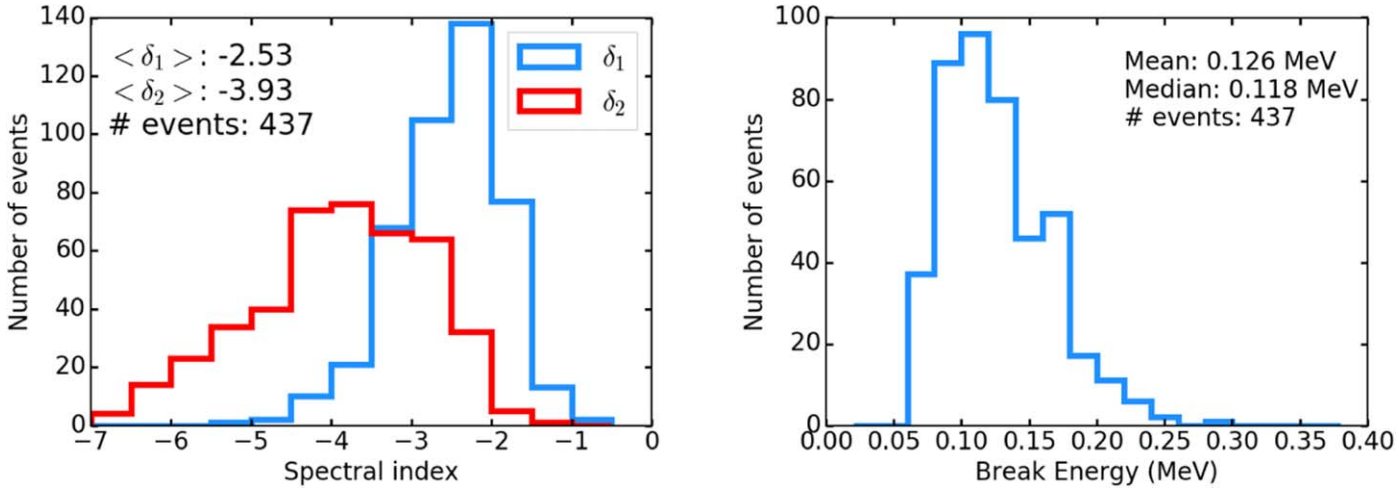

Figure 4. Spectral indices for broken-power-law events (left) and corresponding break energies (right).

found a harder δ_1 and a smaller break energy. Especially when comparing our values of δ_1 and δ_2 of the impulsive sample (see Table 1), we found significantly softer values than Krucker et al. (2009), which might be caused by the weaker solar cycle 24 but could also be due to the different instrumentation and their nonequal energy ranges used in the studies. We found a mean break energy of $E_b = 126 \pm 56$ keV while Krucker et al. (2009) found a break energy of about 60 keV. Note, however, that the SEPT measurements and our fitting procedure only allowed a spectral break between $\gtrsim$70 and $\gtrsim$300 keV to be determined, which will presumably also impact the range of δ_1.

To be able to analyze all events in our sample together, regardless of their spectral shape or the position of the eventual break point, we define two spectral indices $\delta 70$ and $\delta 200$, corresponding to the spectral index found in the energy range around 70 and 200 keV, respectively. In the case of single power-law events, $\delta 70$ and $\delta 200$ have equal values. For double power-law events, defined by the two spectral indices δ_1 and δ_2, we define $\delta 70$ and $\delta 200$ as follows:

$$\begin{aligned}\delta 70 &= \delta_1 \ : E_b > 70\text{keV}\\ \delta 70 &= \delta_2 \ : E_b < 70\text{keV}\\ \delta 200 &= \delta_1 \ : E_b > 200\text{keV}\\ \delta 200 &= \delta_2 \ : E_b < 200\text{keV}.\end{aligned}$$

These two energies, 70 keV and 200 keV, lie outside most of the break energies for the broken-power-law events (see Figure 4 right) so that for most of those events, $\delta 70$ ($\delta 200$) represents δ_1 (δ_2). The corresponding distributions of $\delta 70$ and $\delta 200$ are shown in Figure 5. The mean spectral indices are $\delta 70 = -2.94 \pm 1.19$ and $\delta 200 = -3.55 \pm 1.45$. The number of events for $\delta 70$ is larger because many events do not extend to energies of 200 keV. Table 1 summarizes the mean values of the spectral indices of $\delta 70$ and $\delta 200$, the single power-law events (δ), the broken-power-law events (δ_1, δ_2), as well as the corresponding break points E_b. The table also provides the widths of the distributions.

Figures 6 and 7 show the same distributions of spectral indices and break energies as in Figures 4 and 5 but for the subsample of impulsively rising events. The mean spectral indices and break points of the impulsive sample are also listed in Table 1. The break point is slightly smaller and all the spectral indices are on average softer when compared to the whole sample. The largest difference applies to δ_2 with a mean spectral difference of 0.85. The smallest average change of 0.33 is observed for δ_1. The distributions of spectral indices are always wider for the impulsive sample.

Table 1
Means of Spectral Indices and Break Energies for All Events and the Impulsive Sample

	All Events			Imp. Sample		
	Mean	Width[a]	#	Mean	Width	#
Total #			781			228
δ (single PL)	−3.47	1.15	344	−3.94	1.42	132
δ_1	−2.53	0.87	437	−2.83	0.82	96
δ_2	−3.93	1.53	437	−4.85	1.57	96
E_b	126 keV	56 keV	437	117 keV	36 keV	96
$\delta 70$	−2.94	1.19	781	−3.47	1.42	228
$\delta 200$	−3.55	1.45	420	−4.22	1.39	94

Note.
[a] The width is determined by the span between the first and third quartiles of the distributions.

3.2. Correlations of Spectral Features and Event Properties

For the broken-power-law events, Figure 8 plots the spectral indices above and below the break against each other with all events on the left-hand side and only impulsive events on the right-hand side. Note that the few outlier events (open symbols), which correspond to an unexpected spectral hardening above the break, have been excluded from the fit and the correlation (provided in the legend). Most of these are events that occurred during periods of ion contamination and the spectral hardening could be due to an undercorrection of the contamination effect. The correlation between δ_1 and δ_2 is smaller for the impulsive sample; however, this could be due to the poorer statistics. Nevertheless, we find a clear linear correlation between the spectral indices of 0.69, which is in agreement to previous results (Krucker et al. 2009), finding a correlation coefficient of 0.61.

Figure 9 displays the difference between the spectral indices below and above the break. The mean difference is larger for the impulsive sample (1.8), which compares better to the results

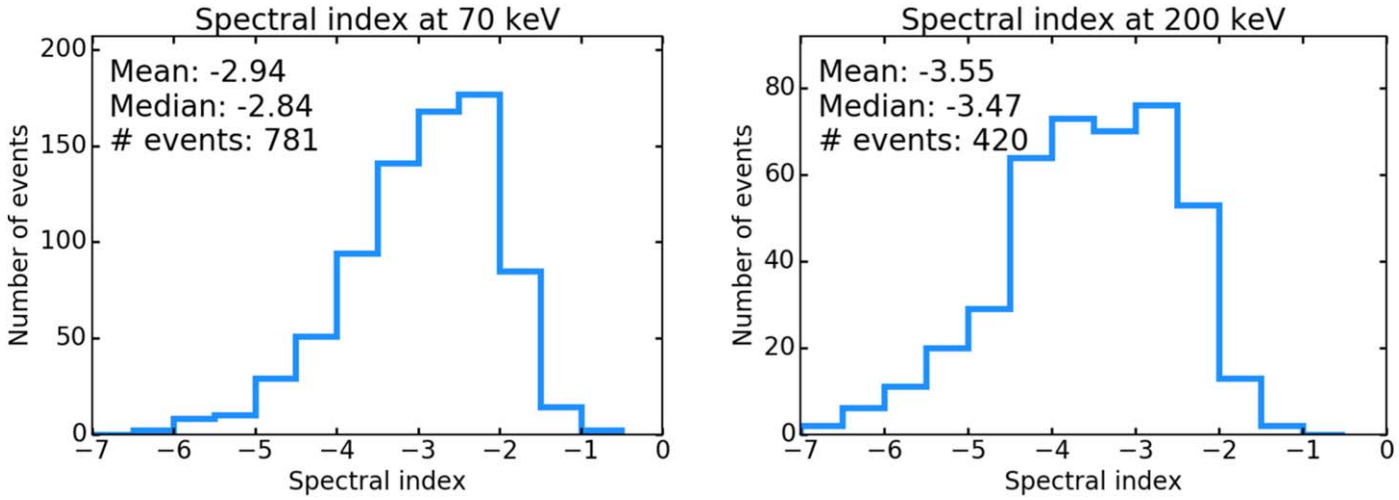

Figure 5. Spectral indices at 70 keV (left) and 200 keV (right) for the whole sample of events.

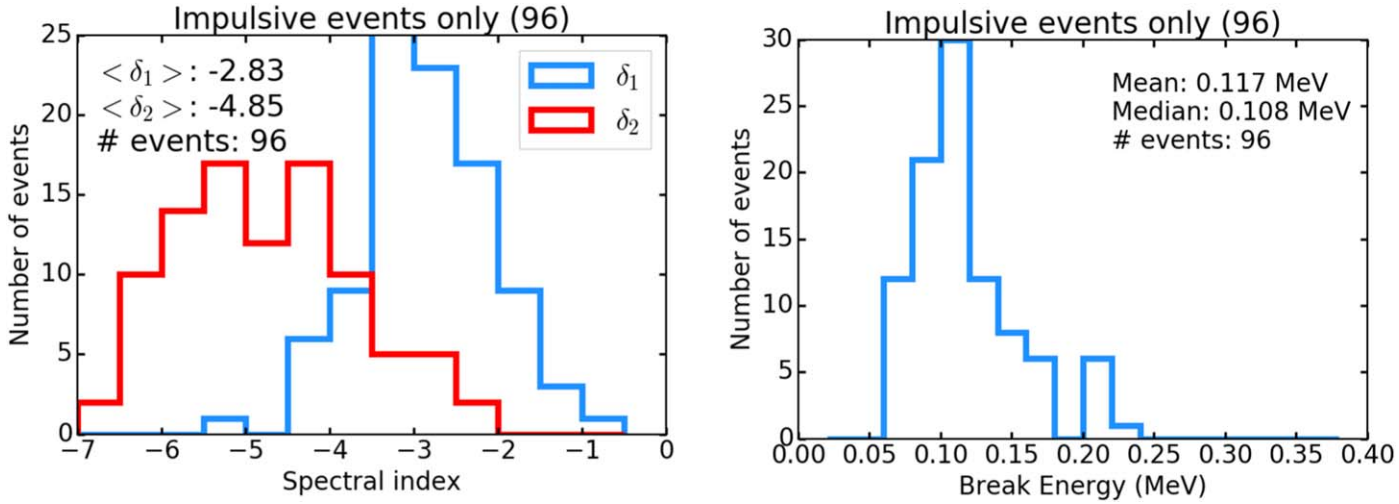

Figure 6. Histogram of power-law indices (left) and break points (right) for the impulsive sample.

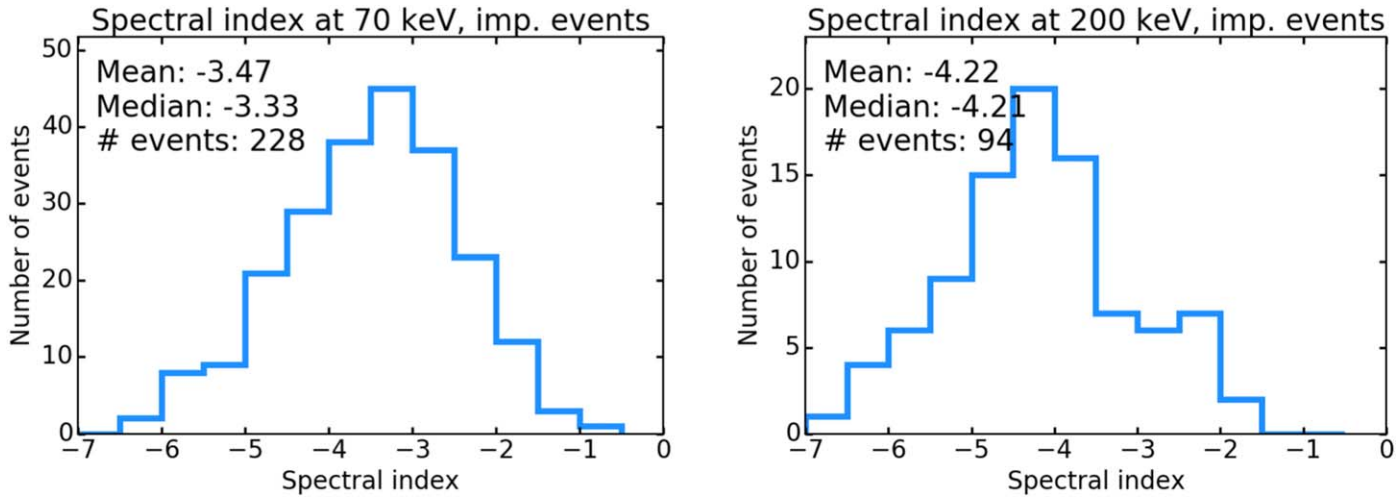

Figure 7. Histogram of spectral indices at 70 and 200 keV for the impulsive sample.

by Krucker et al. (2009), who found a mean difference of 1.7 for their sample of 62 impulsive events.

Figure 10 plots the break energy of the broken-power-law events as a function of the intensity at the break energy and shows that there is no correlation. The values of break energies are rather equally distributed around the mean value. The grouping of points in columns reflects the limitation of the break-point determination caused by the energy binning of the instrument.

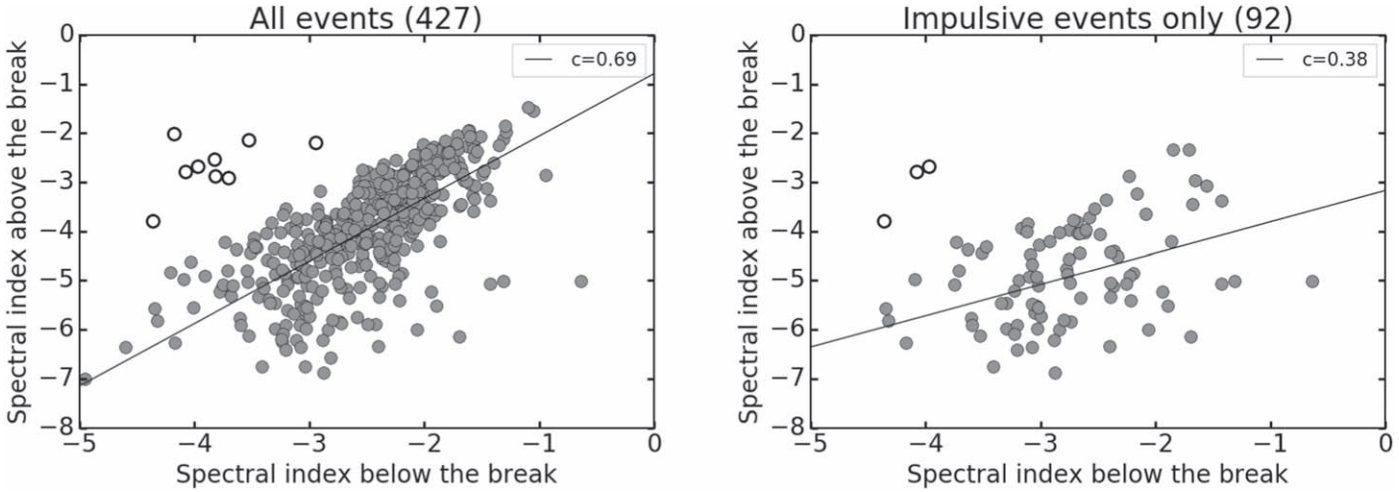

Figure 8. Spectral index above the break as function of the spectral index below the break for all broken-power-law events. Left: all events in the sample, right: only events with impulsive rises. The black line represents a linear regression and the Pearson correlation coefficients are provided in the legend. Note that events showing a spectral hardening above the break (open symbols) have been excluded from the correlation.

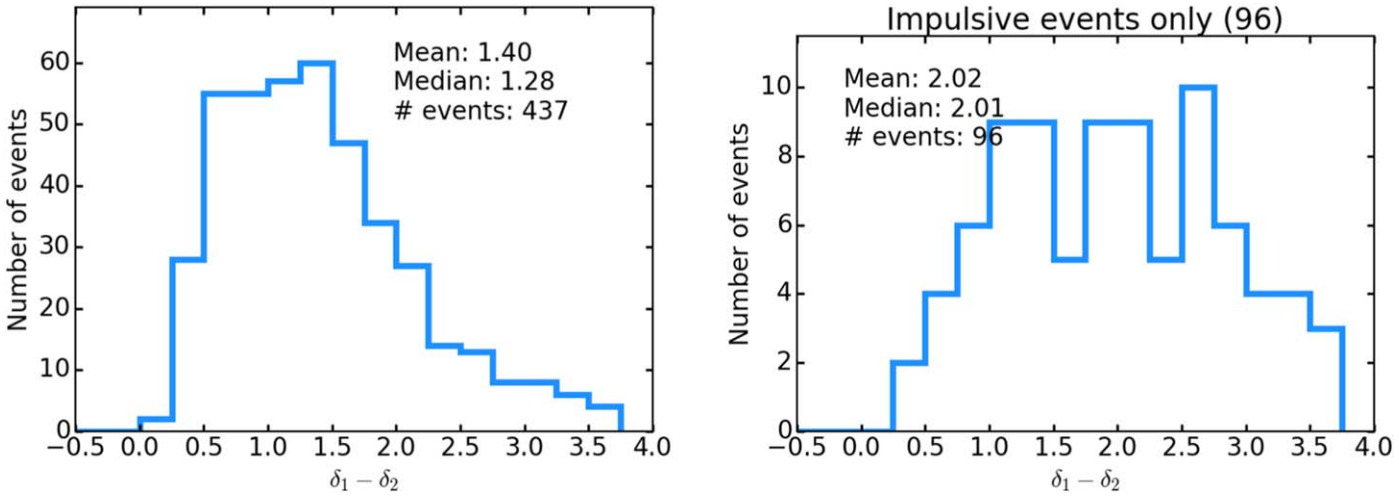

Figure 9. Difference between spectral index below the break and above the break for all events (left) and impulsive events only (right).

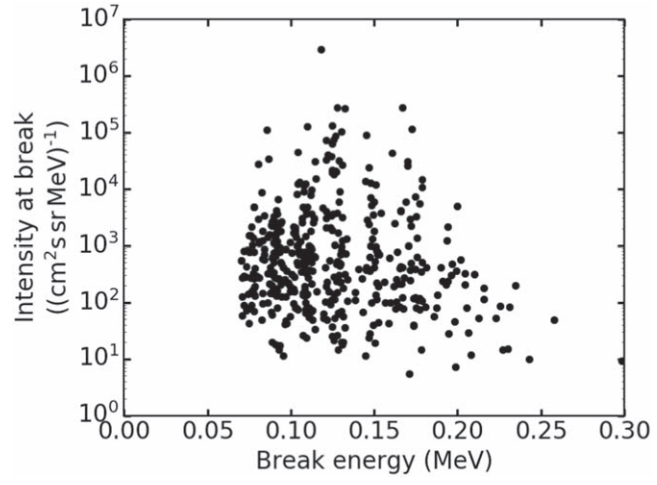

Figure 10. Break energy as a function of the intensity at the break energy (pre-event background subtracted) for all broken-power-law events.

Figure 11 shows the histogram of rise times (times from onset to peak time) with 10 minute binning in gray. While the main plot zooms in to rise times between 0 and 400 minutes, the inset shows the whole histogram, revealing that a few events show rise times of even some days. A few of these extremely long rising events are accompanied by a CME, driving a shock, with comparable timescales of the electron rise and the CME propagation suggesting that the CME-driven shock could be the main source for those events. However, most of the very long rise time events are showing only very small intensity increases and are not accompanied by an in situ passage of a shock. The colored bars show the number of events in the corresponding bin, which have a spectral index $\delta 70$ softer (red) or harder (blue) than -3.5. While softer events cluster more at small rise times ($<$20 minutes), although constituting only about half of all events, the harder-spectra events dominate at longer rise times. Above the second bin ($>$20 minutes), the number of events per bin is significantly smaller and decreases gradually. We, therefore, choose the limit for impulsive and nonimpulsive events (see Section 3) to be at 20 minutes, marked by the dashed line.

A more detailed view on this dependence is shown in Figure 12 displaying the rise times as a function of the spectral index at 70 keV ($\delta 70$). While the variation of rise times is very small for events with soft spectral indices ($\delta 70 \lesssim -4$), being

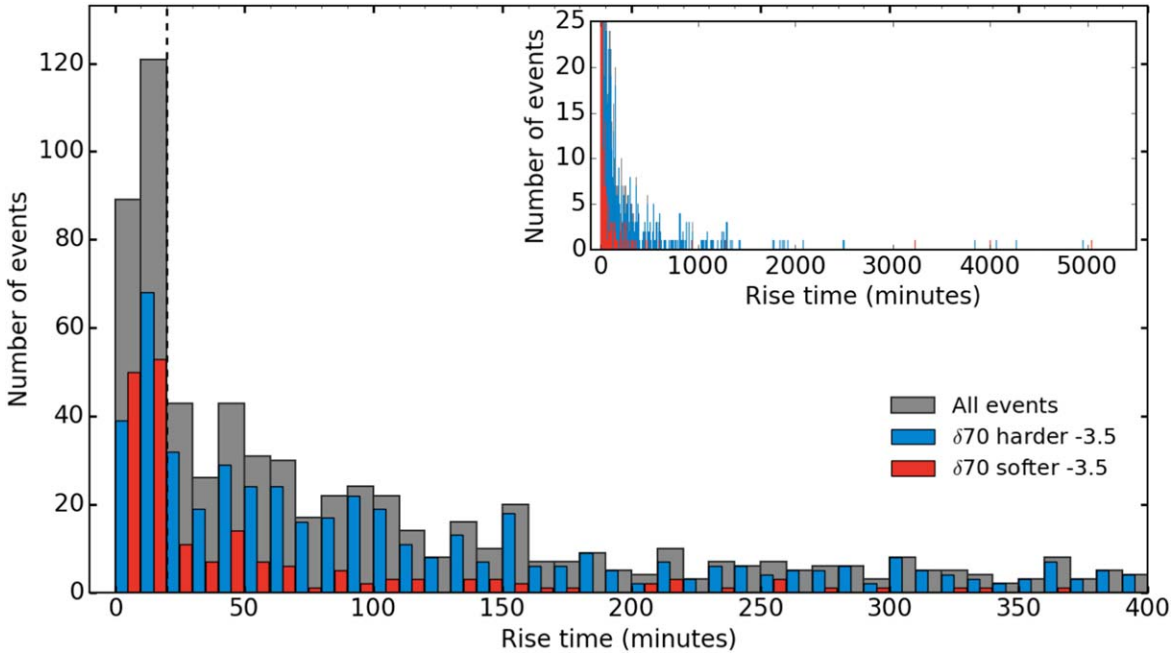

Figure 11. Histogram of rise times of all events (gray) with a 10 minute binning zoomed in to 0–400 minutes. The colored histograms divide the sample of all rise times based on the correspondingly measured spectral index $\delta 70$. The number of events with harder spectra ($\delta 70 > -3.5$) is plotted in blue and the one with softer spectra ($\delta 70 < -3.5$) in red. The inset at the top right shows the histograms zoomed out on the x-axis but zoomed in on the y-axis where the histogram of soft-spectra events (red) is plotted on top of the one with the hard-spectra events (blue) and the histogram of all events (gray) in the back.

almost exclusively impulsive, a large variation of rise times is observed at the harder-spectra side with $\delta 70 \gtrsim -3.5$. The separation of events into soft- and hard-spectra events, used in this study, is driven by this difference in the variation of rise times using a limit of $\delta 70 \sim -3.5$. Spectra associated with long rise time (gradual) events are almost exclusively hard ($\delta 70 \gtrsim -3.5$). Furthermore, the distribution there seems to be limited toward the left-hand side, being caused by the absence of soft-spectra events with longer rise times. Figure 13 plots the same dependence on a logarithmic scale (to emphasize the short rise time events) in the top panels with $\delta 70$ on the left and $\delta 200$ on the right. Figure 14 shows the same for the broken-power-law events with δ_1 on the left and δ_2 on the right, respectively. The bottom panels show the corresponding distributions of the peak intensities at 55–85 keV (with pre-event background subtracted), which show the highest values preferentially during hard-spectra events (upper-right corner). The majority (90%) of the very high intensity events, with peak intensities $I > 1e4$ belong also to the nonimpulsive group (not shown). The lower limit of the peak intensity distributions (bottom panels, lower -left corner) is defined by the detection limit of the instrument with the downward slope (from soft to hard spectral indices) being caused by small and soft events being less likely to be detected as the higher energies will then be hidden in the instrumental background. Furthermore, as the event list is based on the energy range of 55–85 keV, very small and soft events, only significantly observed below that energy, do not appear in the sample. The limit at the upper-left side of the distribution is not instrumental and is much sharper for $\delta 70$ (Figure 13, left) than for $\delta 200$ (Figure 13, right). Its cause is, however, not clear (see Section 4). The colored points in Figure 13 denote the presence of MeV electrons as measured by *STEREO*/HET in its three electron channels. The plotted color (see figure legend) marks the highest HET energy bin, where a corresponding event was observed. The HET events

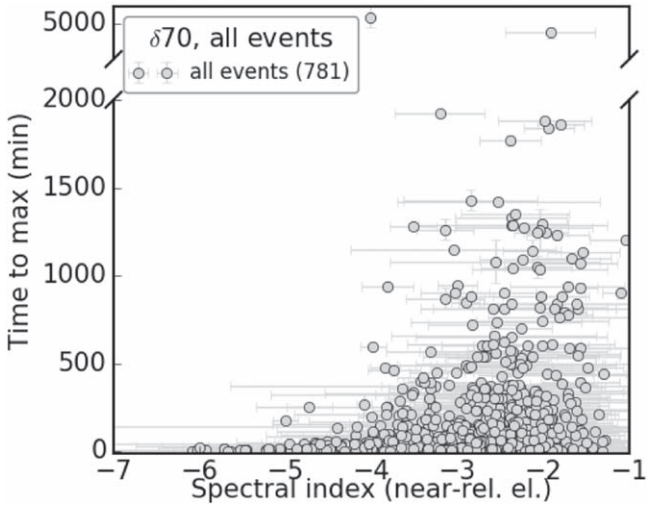

Figure 12. Rise times (time from onset to maximum) of all 55–85 keV electron events in the SEPT electron event list as a function of the spectral index at 70 keV ($\delta 70$).

have been identified as significant (3σ) increases above the pre-event background in temporal coincidence with the respective SEPT event. These high-energy electrons mainly occur during the very intense and hard-spectra events, representing the events with more efficient acceleration, i.e., producing more and higher-energy electrons. A total of 23% of the NR electron events are accompanied by 0.7–1.4 MeV electrons while only 12% show an increase in the highest HET channel of 2.8–4 MeV.

Figures 15 ($\delta 70$) and 16 ($\delta 200$) separate the events into those with (left) and without (right) an accompanying high-energy proton event as indicated by a coincidental increase (of 5σ above pre-event background) in the 60–100 MeV proton channel of *STEREO*/HET. The fraction of NR electron events which are accompanied by 60–100 MeV protons is 11%. The events with

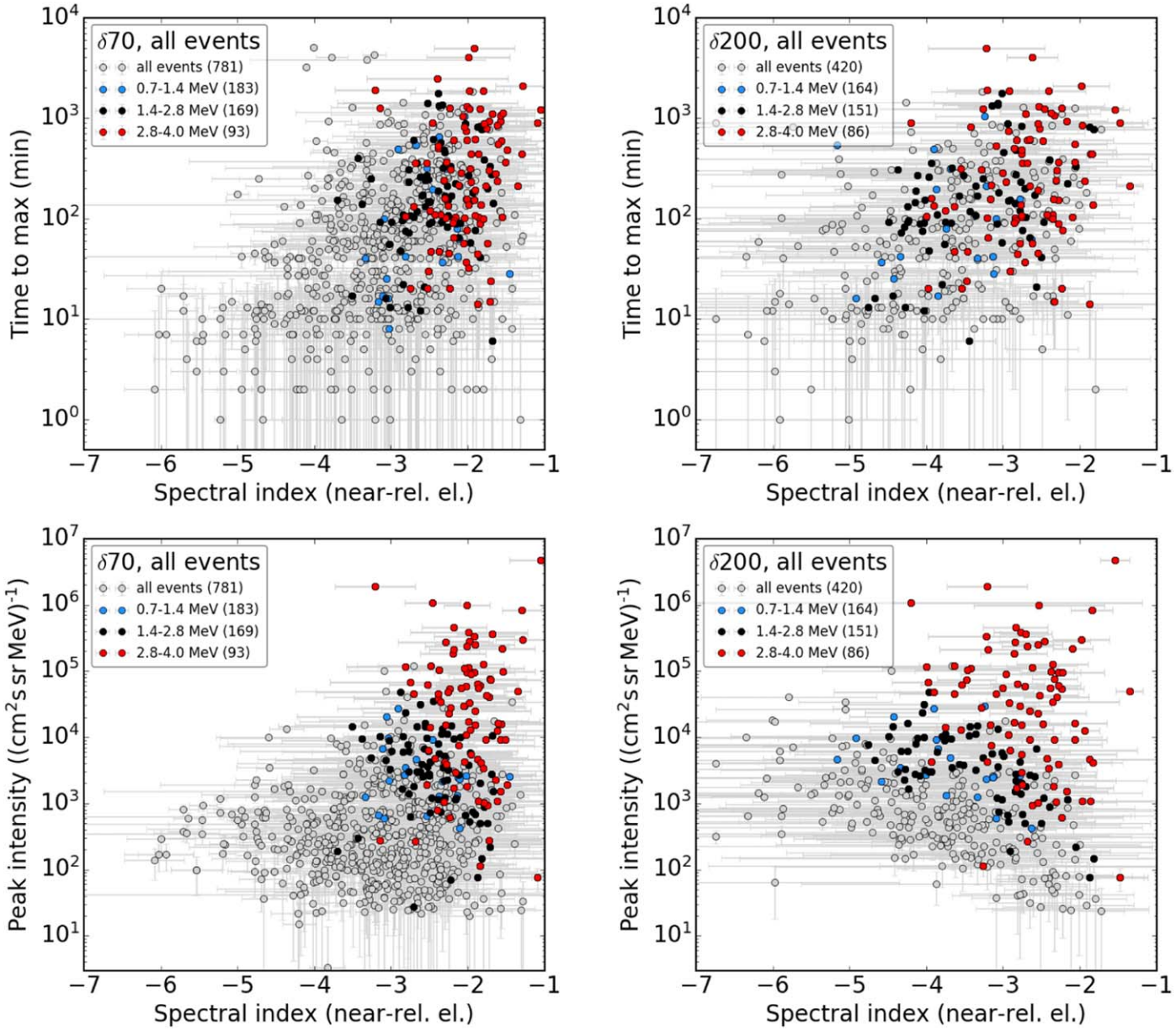

Figure 13. Rise times (top) and peak intensities (bottom) at 55–85 keV (pre-event background subtracted) as a function of the spectral index (gray points) at 70 keV (left) and 200 keV (right). The colored points mark those events where electrons in the MeV range (measured by *STEREO*/HET) were also present, with red denoting that the highest HET channel (2.8–4 MeV) was populated, black meaning that only energies up to the second channel (1.4–2.8 MeV) were observed, and blue only in the first HET channel (0.7–1.4 MeV).

accompanying 60–100 MeV protons (left sides) only populate regions of harder spectral indices. Furthermore, most of the highest (55–85 keV) peak intensities in the sample belong to those events accompanied by 60–100 MeV protons. Almost no solely NR electron event, not detected in the HET electron range (gray points), is observed when the high-energy protons are present. Also, most of the MeV electron events (colored points) and especially most of the highest-energy electrons (red points) appear on the left-hand sides for both (δ70) and (δ200). On the right-hand sides of Figures 15 and 16 (where 60–100 MeV protons are not present), the MeV electrons accompany the NR electrons in only 15% of the events.

In the same manner as Figures 15 and 16, Figures 17 and 18 show the events for cases when a type II radio burst was present (left) and when not (right) are separated. The information on the presence of the type II bursts is taken from the CDAW type II and CME list,[9] which is based on *Wind*/WAVES and *STEREO*/WAVES data, allowing the type II burst to occur up to 2 hr before the electron onset. Because the above list is not comprehensive and contains large gaps, we further complement our list by the type II bursts identified by Richardson et al. (2014; based on the *WIND*/WAVES list[10]) for >25 MeV proton events if these accompany our electron events. Because the source locations have not been identified for most of the electron events, the 25 MeV proton event list is also used to provide the source locations for a subset of events. Figures 17 and 18, therefore, mainly plot the subsample of our electron events, which are also accompanied by >25 MeV protons. The events with type II radio bursts (left sides of

[9] https://cdaw.gsfc.nasa.gov/CME_list/radio/waves_type2.html
[10] https://solar-radio.gsfc.nasa.gov/wind/data_products.html

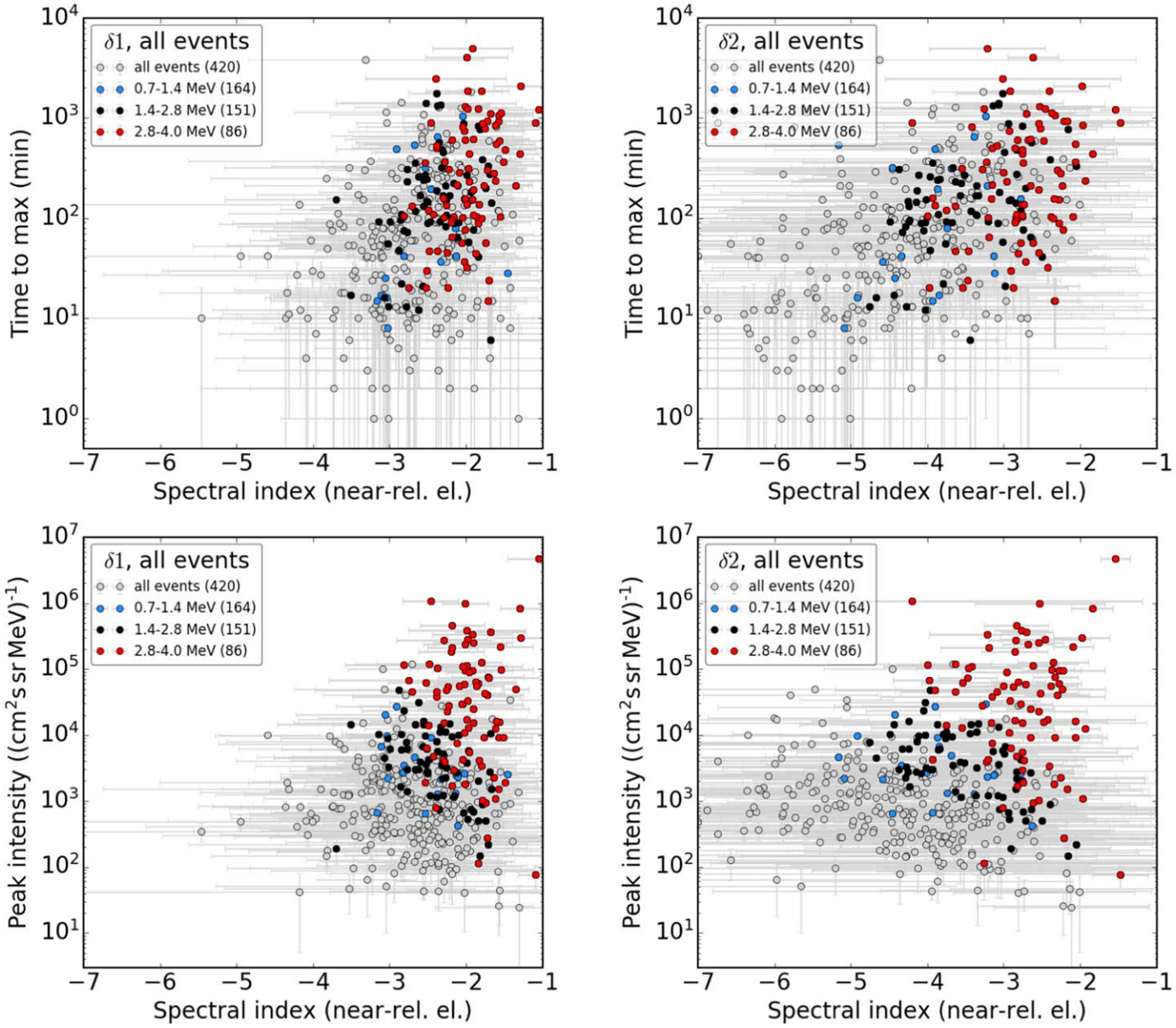

Figure 14. Similar to Figure 13, but for broken-power-law events only with δ_1 shown on the left-hand side and δ_2 on the right.

Figures 17 and 18) tend to show the highest peak intensities in the sample. A fraction of about 73% of these events is also accompanied by MeV electrons, while this is only the case for 58% of the events without type II bursts (Figures 17 right). However, there is no striking difference between the distributions with and without type II bursts, which is most likely due to the bias of the reduced sample of events, where most of the plotted events are accompanied by >25 MeV protons.

For the same reduced sample, Figure 19 plots the spectral indices δ70 and δ200 as functions of the longitudinal separation angle between the parent flaring active region and the magnetic footpoint longitude of the spacecraft. The latter one was determined with a ballistic backmapping to the solar source surface, taking into account the observed solar wind speed. The solar source locations of the events are provided by Richardson et al. (2014). There is no striking dependence for either δ70 or δ200 on the separation from the parent source region at the Sun. However, for δ200, the softest spectra ($\delta \sim -4$) events tend to cluster at well-connected positions (separation angles $\lesssim$60°).

3.3. Multispacecraft Events

For those events that were accompanied by >25 MeV protons, we selected all events observed by both *STEREO* spacecraft. Figure 20 (top) shows the spectral indices δ70 of the multispacecraft events (points connected by lines) as a function of the longitudinal separation angle. Widespread events, meaning events where the observers are either separated by more than 80° or where one observer is separated more than 80° from the parent flare site, are marked in black while the narrower events are plotted in gray. However, every point must be taken as a lower limit as the actual event may be wider than the range covered by the spacecraft. The bottom panel shows the spectral index change within each event from the better-connected spacecraft to the worse-connected one as a function of the absolute longitudinal separations of each spacecraft to the parent flare. Most of the

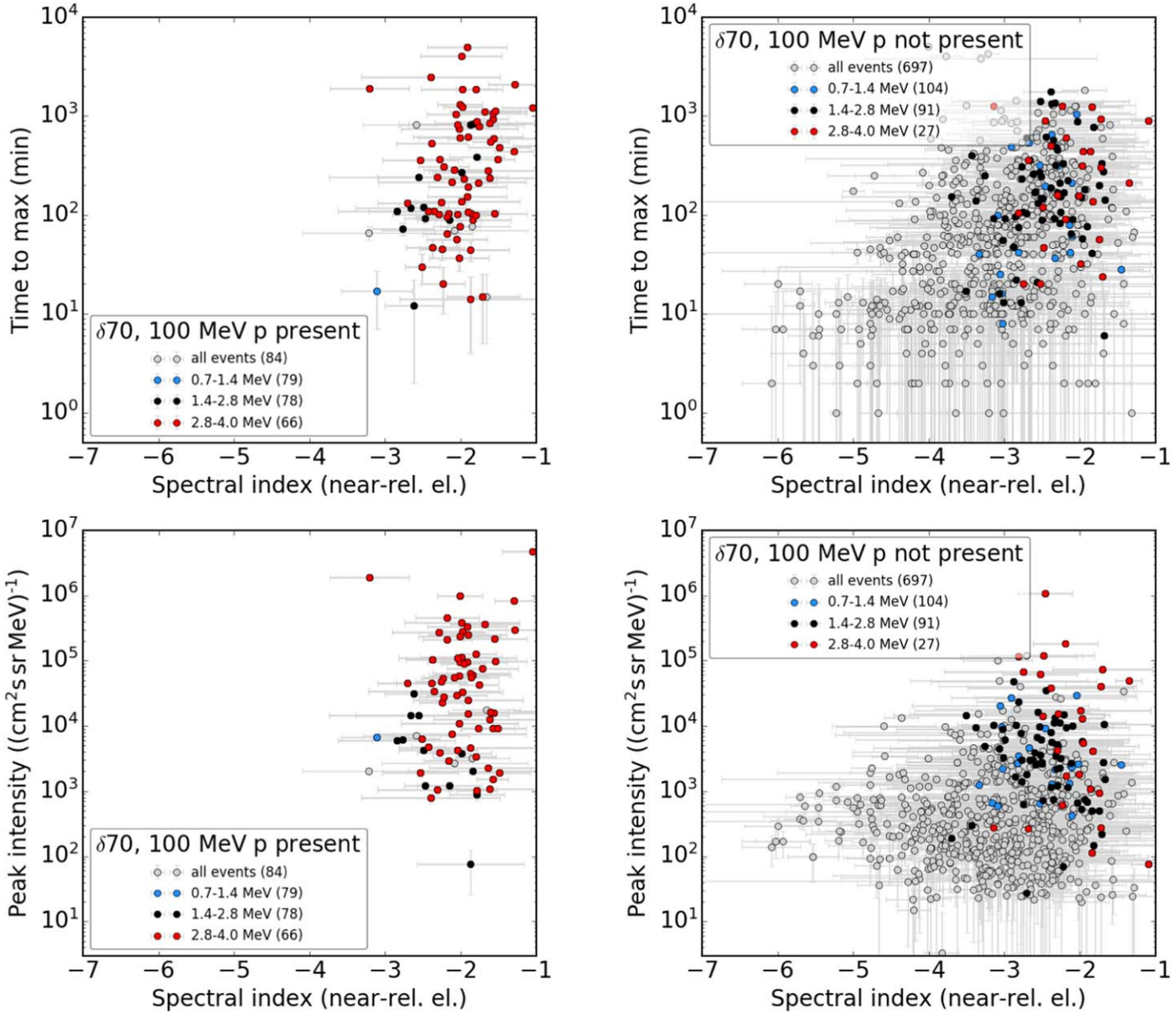

Figure 15. Rise times (top) and peak intensities (bottom) at 55–85 keV as a function of the spectral index at 70 keV. The left figure shows only events where 60–100 MeV protons were present, and the right figure where these were not present.

events show a spectral softening (for $\delta 70$) toward larger separation angles (negative spectral change). For the spectral index at 200 keV, we do not find such a difference but the numbers of events with softening or hardening are almost equal (not shown). The average spectral index for the multispacecraft events ($\langle \delta 70 \rangle = -2.18$) is harder than the mean of the whole sample ($\langle \delta 70 \rangle = -2.94$), and the widespread sample shows an even harder mean ($\langle \delta 70 \rangle = -2.07$) than the narrow-spread sample ($\langle \delta 70 \rangle = -2.44$). However, the strong event-to-event variations result in widths of the distributions of the spectral index of about 0.7 to 1.1 (as defined like in Table 1). Because of that, together with the low statistics of the multispacecraft sample, this apparent spectral hardening must be taken with caution.

4. Discussion and Conclusions

The presented study draws a comprehensive picture of the spectra of NR solar electron events in solar cycle 24 at 1 au. As the event selection was only driven by the significance level of the electron increases, no bias is present, other than the instrument sensitivity and limitations, which would favor certain types of events. For the whole sample of events (781), we find hard mean values of the analyzed spectral indices (see Table 1) with values of $> \langle \delta \rangle > -3$ at lower energies (e.g., δ_1, $\delta 70$) and values of $-7 \langle \delta \rangle > -4$ at higher energies (e.g., δ_2, $\delta 200$). All spectral indices in our sample vary within $-7 < \delta < -1$ The mean values soften when only the 228 impulsively rising events (with rise times smaller than 20 minutes) are selected. Rise times up to 20 minutes are the most likely ones in the distribution of rise times of our sample (see Figure 11). These impulsive events do, however, only account for about one quarter of all events in the sample.

A broken-power-law spectrum has been reported for impulsive solar electron events (e.g., Lin et al. 1982; Lin 1985; Krucker et al. 2009), and we find such a spectral shape for about half of the events in our sample and for one-

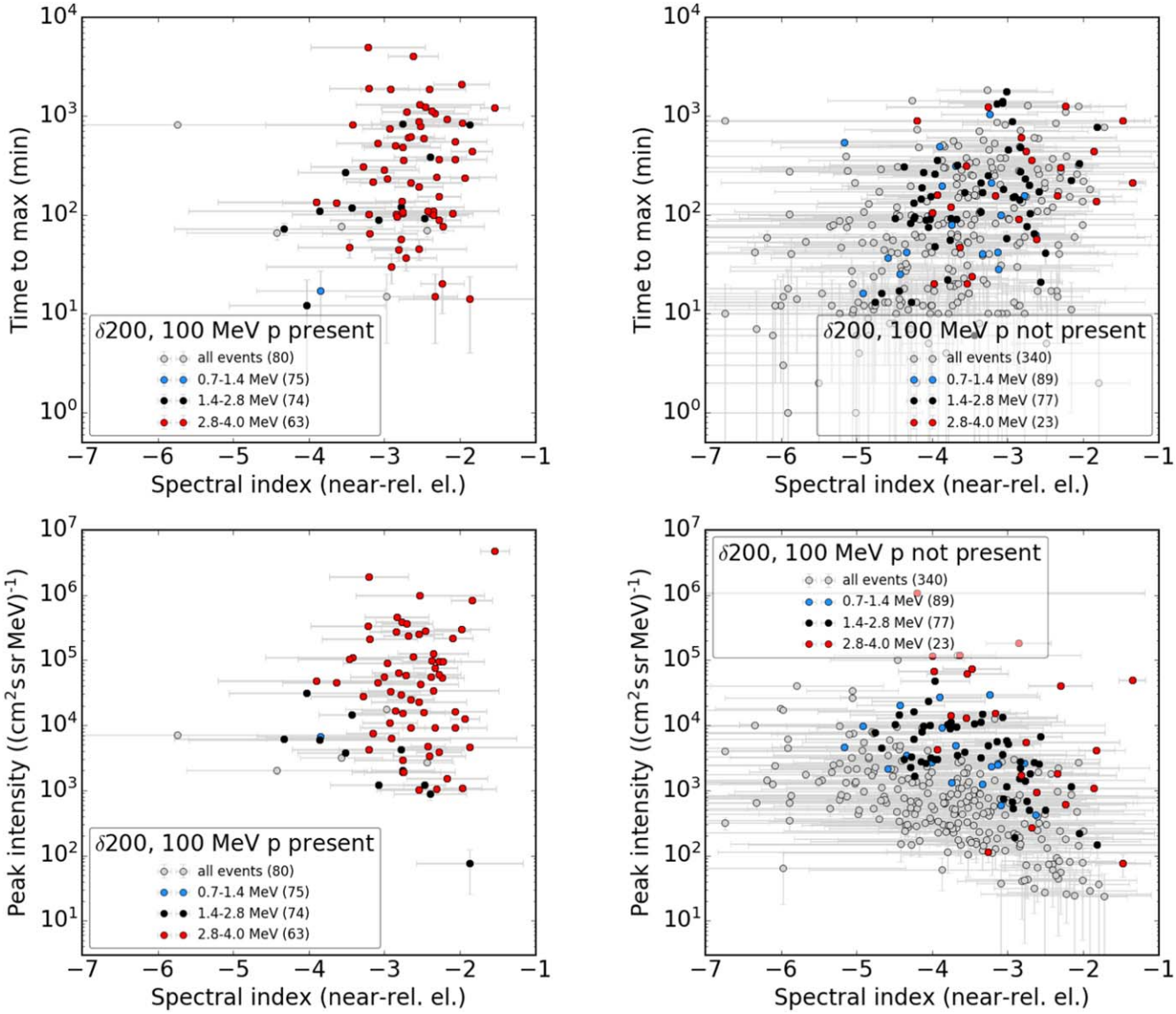

Figure 16. Similar to Figure 15, but for the spectral index at 200 keV.

third of the impulsive group. In case of the events showing a single-power-law shape, it is not clear if these are really pure power-law spectra or if a potential break point lies outside the detected energy range or outside the range where we are able to detect a break point ($70\,\mathrm{keV} < E_b < 300$ keV) based on the instrument limitations and our fitting procedure.

While Krucker et al. (2009) argued that the origin of the spectral break could either be the acceleration process itself, a secondary process, such as the escape from the acceleration site, or transport effects, Kontar & Reid (2009) found that plasma wave generation by electrons below 100 keV during their propagation from the Sun causes a spectral break. This is because the energy loss of the electrons leads to a flattening/hardening preferentially of the low-energy part of the spectrum. The break point around 35 keV at 1 au found by Kontar & Reid (2009) agrees reasonably well with the mean spectral break of $E_b = 60$ keV (ranging from 30 to 100 keV) found by Krucker et al. (2009). Our study finds a significantly higher break point of about 120 keV. Furthermore, a prediction of the energy-loss process due to wave generation (Kontar & Reid 2009) is that the break energy should be correlated with the intensity at the break. However, such a correlation is not observed in the present study (Figure 10). This suggests that the spectral breaks, found in our study, are not formed by the energy-loss process due to wave generation. Generally, every energy-loss process could lead to the formation of a spectral break. Dalla et al. (2015) studied the effect of adiabatic cooling of solar energetic protons and noted that particle drifts significantly contribute to this deceleration effect, with larger relative energy losses for lower-energy particles. Although the drifts for electrons will be rather small, a significant relative energy loss could still be the result that provides another potential mechanism for a spectral break. In addition to energy-loss processes, a particle-loss process could be a further reason for a spectral break. Such a particle loss could be caused by preferential particle scattering at magnetic irregularities off the connecting magnetic field line. The presence of such energy-dependent scattering was found by Dröge (2000) and Agueda et al. (2014) through energy-dependent transport modeling of SEP events, showing that the mean free path of NR electrons decreases with increasing energy. The higher-energy electrons therefore experience stronger scattering than the lower-energy

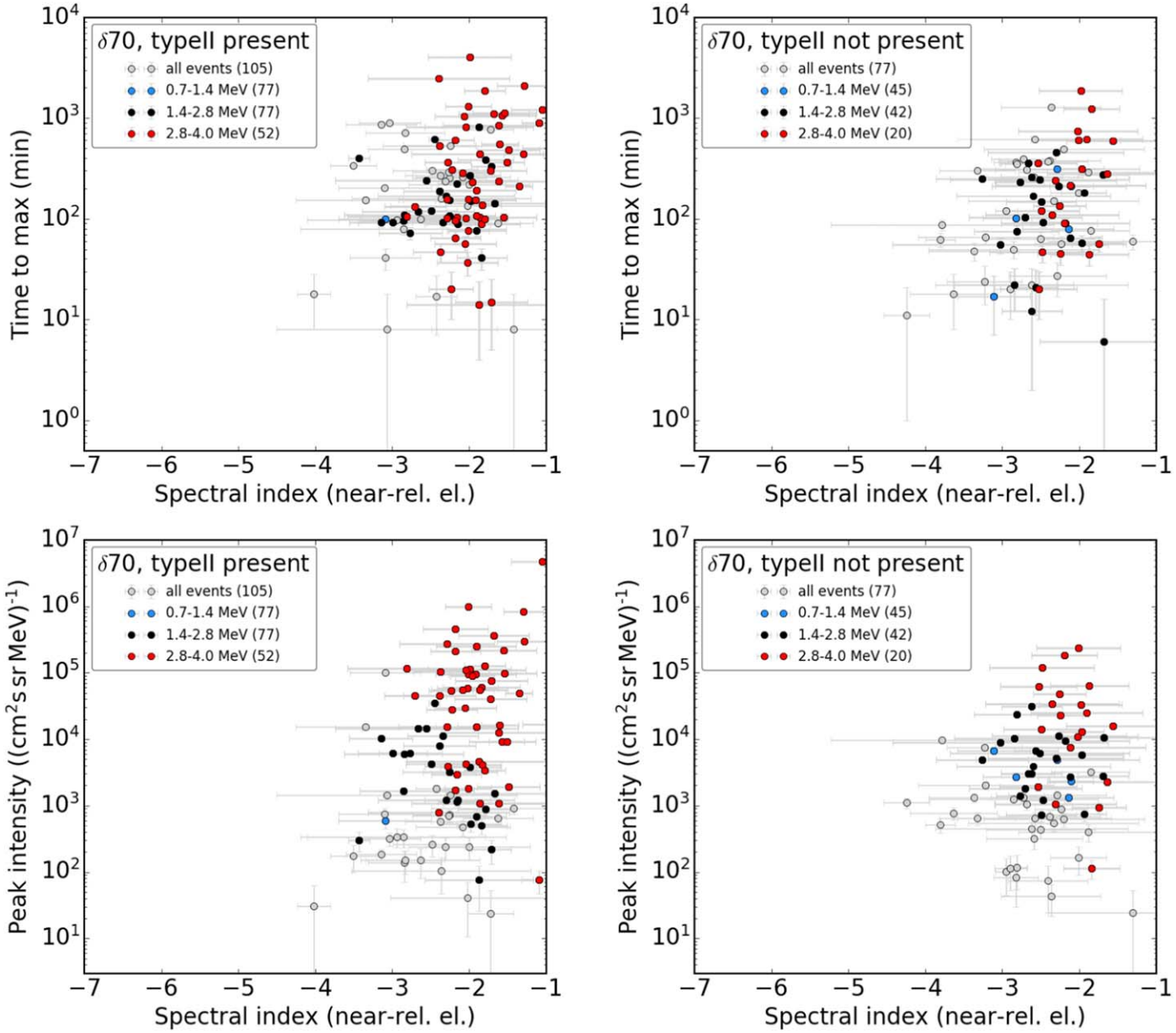

Figure 17. Rise times (top) and peak intensities (bottom) at 55–85 keV as a function of the spectral index at 70 keV. The left (right) figure shows only events that were (not) accompanied by type II radio bursts. This plot only includes those events, which were accompanied by >25 MeV protons.

ones up to a constant mean free path above ~1 GV (~1600 keV). For electrons propagating from the Sun to an observer at 1 au, this effect could result in a depletion of the high-energy component because these particles were scattered off (or back along) the connecting field line. However, it is not clear yet if the potential mechanisms mentioned above would indeed manifest as a spectral break or only as a systematic change of the single power law. Other observational studies (e.g., Lin et al. 1982; Lin 1985) also found break points at higher energies of 100 to 200 keV. We therefore suggest that the break point itself and the potential presence of various break points, e.g., one at $\gtrsim$100 keV and one at $\lesssim$60 keV, might be caused by different processes or a combination of those as discussed above. However, one has to keep in mind that the determined spectral values can be influenced by the fitting range and/or the energy limits and binning of the employed instrument. Our fitting method, applied to SEPT data, limits the break energy to be found between ~70 and ~300 keV. However, the energy binning of SEPT is finer than that of *Wind*/3DP employed by Krucker et al. (2009).

We find a strong variation of rise times for our 55–85 keV electron events ranging from minutes up to days (see Figure 11). Those events showing short rise times appear consistent with being caused by solar flares, which involve a short-duration (of the order of minutes) acceleration and IP injection. The events with long rise times, however, need a further process to be involved. On the one hand, a gradual rise can be caused by strong particle diffusion in the IP medium, even if the injection at the Sun is very short. However, transport modeling of NR solar electron events usually reveals rise times of the order of a few hours, even if the scattering or (perpendicular) diffusion is very strong (see Dresing et al. 2012; Agueda et al. 2014; Dröge et al. 2014, 2016). Furthermore, these processes will reduce the peak intensity

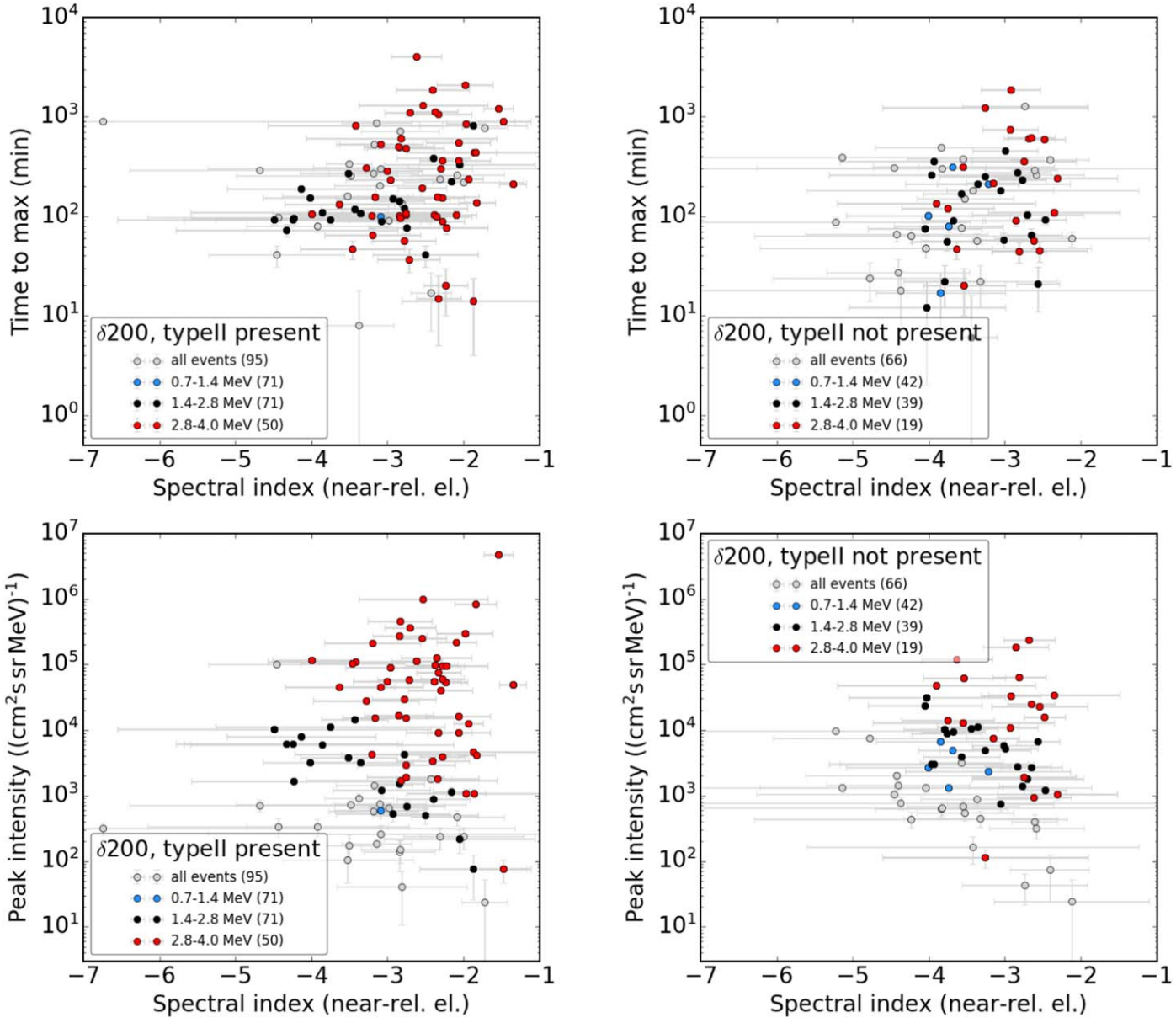

Figure 18. Same as Figure 17, but for the spectral index at 200 keV. This plot only includes those events, which were accompanied by >25 MeV protons.

by smearing out the impulsive shape of the distribution on the one hand and by particle loss due to perpendicular diffusion on the other hand. Because the events with long rise times include some of the largest-intensity events, this also suggests that diffusive transport is not the main process responsible for long rise times. Furthermore, diffusive transport should be equally present for all events not depending on their spectral index. So, the absence of longer rise times during soft-spectra events further suggests that the electron diffusion effect is not the most dominant process determining the observed rise times. Another mechanism responsible for long rise times is a long-lasting acceleration and/or IP injection of the electrons. The observed correlation of harder spectra (e.g., $\delta 70 \gtrsim -3.5$) with longer rise times, and the additional presence of higher-energy (0.7–4.0 MeV) electrons for these events (see Figure 13), shows that the very long rise time events are associated with a more efficient acceleration process, yielding higher energies/harder spectra. And this acceleration process must involve a long-lasting electron acceleration or IP injection.

The distribution of peak intensities as a function of the spectral index shows a limit toward the upper left with an increasing slope from soft to hard spectral indices (see Figures 13 and 14). This limit is sharper for the spectral index at lower energies (e.g., $\delta 70$ or $\delta 1$). The reason for this limit is not clear. A potential explanation would be the effect of energy loss of the lower-energy part in the spectrum due to wave generation as discussed above. The higher the electron intensity, the larger the wave excitation and, therefore, the energy loss, which would cause stronger spectral hardenings of the low-energy part with increasing peak intensity. However, the missing correlation of the break energy with the intensity (Figure 10) suggests that this effect is not visible in our spectra, probably because SEPT does not cover low enough energies.

The association of our long rise-time and hard-spectra events with the presence of 60–100 MeV protons (Figure 15 and 16) might suggest a common acceleration process for high-energy protons and MeV electrons, with the most favorable candidate being the CME-driven shock. We therefore plot the same

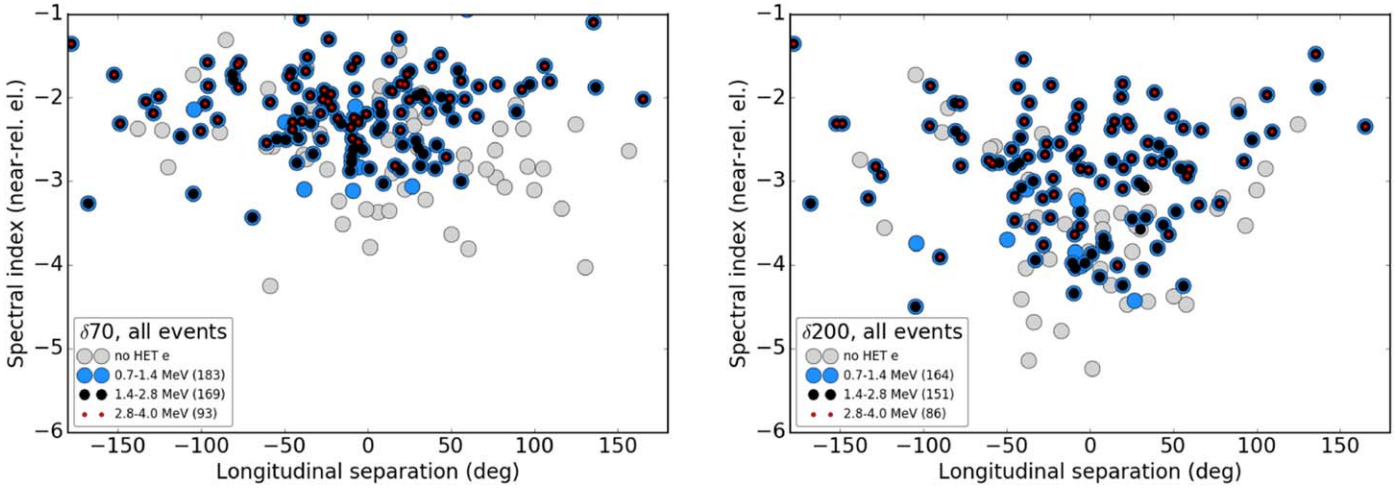

Figure 19. Spectral index at 70 and 200 keV (left and right) as a function of the separation between the flaring region and the backmapped magnetic footpoint longitude of the spacecraft. This plot only includes those events, which were accompanied by >25 MeV protons. Colored points denote the presence of MeV electrons.

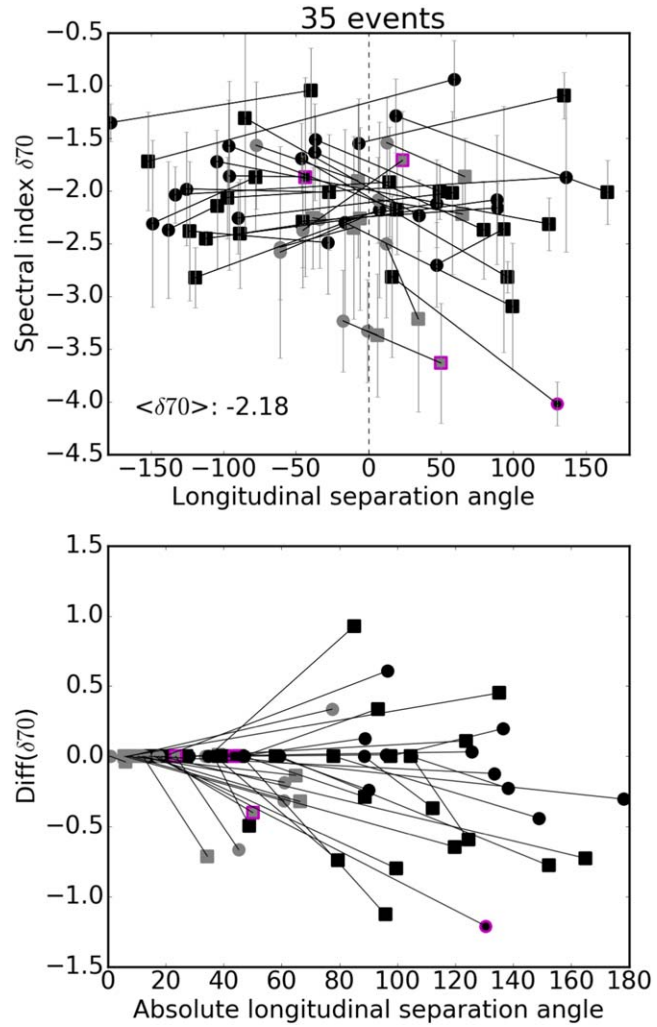

Figure 20. Top: spectral index at 70 keV as a function of the separation between the flaring region and the backmapped magnetic footpoint longitude of the spacecraft for the multispacecraft events. Gray (black) points mark narrow-spread (widespread) events. Magenta borders mark impulsive events. Bottom: spectral change from better-connected spacecraft to a worse-connected one for the same sample of events as a function of the absolute longitudinal separation angle. A negative (positive) change marks a spectral softening (hardening) toward larger separations.

distributions, distinguishing by the presence or absence of a type II radio burst in Figures 17 and 18. However, here we only take into account those events, where a type II burst was either reported in the (incomplete) CDAW type II list or by Richardson et al. (2014), meaning that a >25 MeV proton event was also present in the latter case. We note that efficient electron acceleration at shocks, especially to energies $\gtrsim$100 keV, still challenges state-of-the-art modeling (e.g., Guo & Giacalone 2015; Trotta & Burgess 2019), suggesting that the simple presence of a shock may not be enough to explain the electron event. The very gradual events showing rise times of $\gtrsim$1000 minutes further challenge the shock acceleration scenario as the shock would have to efficiently accelerate the NR electrons over distances of about half an astronomical unit, which is not expected based on in situ observations of shock crossings at 1 au where the shock is very inefficient in accelerating NR electrons (e.g., Dresing et al. 2016; Yang et al. 2019). However, a few of the very long rise-time events ($\gtrsim$1.5 days) of our sample are accompanied by a CME driving a shock where the timescale of the shock propagation to 1 au roughly fits the electron event rise time. These events might be extreme cases and are subject to future investigations. Other possible scenarios accounting for the hard-spectra and long rise-time events of our study are ongoing acceleration in postflare loops (Klein et al. 2005), or reacceleration of flare particles in the CME environment (Petrosian 2016), which could involve the presence of a shock. More complex scenarios involving interacting CMEs (Gopalswamy et al. 2004; Li et al. 2012), the presence of magnetic traps (Kocharov et al. 2017; Dresing et al. 2018) or particle mirrors (Kallenrode & Cliver 2001a, 2001b), and consequently enhanced turbulence levels (Xiong et al. 2006) may play a role in understanding how solar energetic electrons are efficiently accelerated and injected into the IP medium.

Finally, we analyzed the spectral indices in terms of a longitudinal dependence. A spectral systematic spectral change with longitudinal separation from the parent source location could either be caused by transport effects in the IP medium or by longitudinal differences of a potentially extended source. However, whether viewed as single-spacecraft (Figure 19) or multispacecraft (Figure 20) events, there is no striking dependence of the spectral index on longitudinal separation. A

slight tendency for softer spectra to be observed for well-connected positions is evident in Figure 19 for the spectral index at 200 keV, which could be caused by these events being associated with a limited region of weaker acceleration. However, our sample is also biased because it only includes events accompanied by >25 MeV protons for which the sources were identified by Richardson et al. (2014). The same is true for multispacecraft events (Figure 20). No systematic spectral change is seen within the same event as a function of the longitudinal separation.

5. Summary

The presented study is a comprehensive analysis of NR electron spectra in the energy range of 45–425 keV observed at 1 au during solar cycle 24 from 2007 to 2018 by the *STEREO* mission. Of these events, 29% show impulsive rise times to peak intensity of <20 minutes, while the majority show longer, nonimpulsive rise times. The events are approximately equally divided between those having single power-law or broken-power-law energy spectra. However, about half of the single power-law events do not extend to high-enough energies to exclude the potential presence of a break point. The mean spectral indices in the lower-energy range around 70 keV and in a higher-energy regime around 200 keV are $\delta 70 = -2.94$ and $\delta 200 = -3.55$, respectively. The spectra are softer for the impulsive group (with rise times < 20 minutes) with $\delta 70_i = -3.47$ and $\delta 200_i = -4.22$. For those events showing a broken power law, we find a mean break energy of $E_b = 123$ keV. We do not find a dependence of the break energy on the intensity, suggesting that this break is not caused by energy loss of the lower-energy part due to interaction with electrostatic waves in the plasma. Were the spectral index dependent on this effect, higher peak intensities should yield higher spectral breaks. This is because a higher electron beam density would cause a faster generation of waves and therefore a stronger interaction between electrons and plasma waves (Kontar & Reid 2009). An analysis of the spectral indices and the rise times of the events reveals:

1. A strong variation of event rise times (from onset to peak intensity) is found ranging from minutes to several days.
2. Soft-spectra ($\delta \lesssim -4$) events almost always show impulsive rise times but the opposite is not true as the presence of impulsive events with harder spectra shows.
3. Long rise-time events are associated with harder spectra while the opposite is not true (there are also impulsive events with harder spectra).
4. The presence of MeV electrons is associated with the hard-spectra and long rise-time events

While it is likely that the impulsive, soft-spectra events are flare-related events, the hard-spectra, long rise-time events cannot be explained by a simple flare scenario but require another or a secondary process which involves prolonged particle injection and leads to more efficient electron acceleration (in terms of energy). We note, however, that a potential CME- or shock-related source cannot be excluded for the impulsive events. However, such potential shock acceleration would have to occur on correspondingly shorter timescales.

We furthermore find a close correlation between the presence of 60–100 MeV protons with those of the MeV electrons: there are almost no NR electron events that are accompanied by 60–100 MeV protons but not also associated with MeV electrons. This result might imply a common acceleration process of the high-energy electrons and protons, or a common ingredient for the acceleration processes. On the other hand, there are a large number of NR electron events not associated with 60–100 MeV protons that still extend into the MeV range.

For a subgroup of events which are accompanied by >25 MeV protons, we find

1. no clear dependence of the spectral index on the presence or absence of a type II burst,
2. no clear dependence of the electron spectral index on the longitudinal separation angle between the spacecraft magnetic footpoint and the parent solar source region, and
3. no clear systematic dependence of the spectral index on the longitudinal separation angle for multispacecraft events.

A future analysis involving additional observations close to Earth or the Sun (e.g., from the *Parker Solar Probe* and *Solar Orbiter*) may shed more light on the possible longitudinal and radial dependence of the spectral index during solar energetic electron events.

The *STEREO*/SEPT, *Chandra*/EPHIN, and *SOHO*/EPHIN project is supported under grant 50OC1702 by the Federal Ministry of Economics and Technology on the basis of a decision by the German Bundestag.

R.G.H. acknowledges the Spanish MICIU/FEDER/AEI for the financial support under project ESP2017-88436-R. I.G.R. acknowledges support from NASA programs NNH17ZDA001N and NH14ZDA001N-LWS, and from the *STEREO* mission. F.E. and N.D. acknowledge support from NASA grant NNX17AK25G. Additional support from an Alexander von Humboldt group linkage program is appreciated. We thank the International Space Science Institute (ISSI) for hosting our team on "Solar flare acceleration signatures and their connection to solar energetic particles." Financial support by the Deutsche Forschungsgemeinschaft (DFG) via project GI 1352/1-1 is acknowledged.

We thank Dr. R. D. Strauss, Dr. E. Kontar, and Dr. A. Warmuth for helpful discussions.

ORCID iDs

Nina Dresing https://orcid.org/0000-0003-3903-4649
Frederic Effenberger https://orcid.org/0000-0002-7388-6581
Bernd Heber https://orcid.org/0000-0003-0960-5658

References

Agueda, N., Klein, K.-L., Vilmer, N., et al. 2014, A&A, 570, A5
Anderson, K. A., Lin, R. P., Martel, F., et al. 1979, GeoRL, 6, 401
Dalla, S., Marsh, M. S., & Laitinen, T. 2015, ApJ, 808, 62
Decker, R. B., Krimigis, S. M., Roelof, E. C., et al. 2005, Sci, 309, 2020
Dresing, N., Gómez-Herrero, R., Heber, B., et al. 2014, A&A, 567, A27
Dresing, N., Gómez-Herrero, R., Heber, B., et al. 2018, A&A, 613, A21
Dresing, N., Gómez-Herrero, R., Klassen, A., et al. 2012, SoPh, 281, 281
Dresing, N., Theesen, S., Klassen, A., & Heber, B. 2016, A&A, 588, A17
Dröge, W. 2000, ApJ, 537, 1073
Dröge, W. 2003, ApJ, 589, 1027
Dröge, W., Kartavykh, Y. Y., Dresing, N., Heber, B., & Klassen, A. 2014, JGRA, 119, 6074
Dröge, W., Kartavykh, Y. Y., Dresing, N., & Klassen, A. 2016, ApJ, 826, 134
Dulk, G. A., Kiplinger, A. L., & Winglee, R. M. 1992, ApJ, 389, 756

Ellison, D. C., & Ramaty, R. 1985, ApJ, 298, 400
Gómez-Herrero, R., Dresing, N., Klassen, A., et al. 2015, ApJ, 799, 55
Gopalswamy, N., Yashiro, S., Krucker, S., Stenborg, G., & Howard, R. A. 2004, JGRA, 109, A12105
Guo, F., & Giacalone, J. 2015, ApJ, 802, 97
Haggerty, D. K., & Roelof, E. C. 2002, ApJ, 579, 841
Haggerty, D. K., & Roelof, E. C. 2009, in AIP Con. Ser. 1183, Shock Waves in Space and Astrophysical Environments, ed. X. Ao & G. Z. R. Burrows (Melville, NY: AIP), 3
Holman, G. D., & Pesses, M. E. 1983, ApJ, 267, 837
Kaiser, M. L., Kucera, T. A., Davila, J. M., et al. 2007, SSRv, 136, 5
Kallenrode, M.-B., & Cliver, E. W. 2001a, Proc. ICRC (Hamburg), 8, 3318
Kallenrode, M. B., & Cliver, E. W. 2001b, Proc. ICRC (Hamburg), 8, 3314
Klein, K.-L., Krucker, S., Lointier, G., & Kerdraon, A. 2008, A&A, 486, 589
Klein, K. L., Krucker, S., Trottet, G., & Hoang, S. 2005, A&A, 431, 1047
Kocharov, L., Pohjolainen, S., Mishev, A., et al. 2017, ApJ, 839, 79
Kollhoff, A., Wraase, S., Heber, B., et al. 2018, CEAB, 42, 7
Kontar, E. P., & Reid, H. A. S. 2009, ApJL, 695, L140
Krucker, S., Kontar, E. P., Christe, S., & Lin, R. P. 2007, ApJL, 663, L109
Krucker, S., Oakley, P. H., & Lin, R. P. 2009, ApJ, 691, 806
Laitinen, T., Kopp, A., Effenberger, F., Dalla, S., & Marsh, M. S. 2016, A&A, 591, A18
Lario, D., Kwon, R.-Y., Vourlidas, A., et al. 2016, ApJ, 819, 72
Li, G., Moore, R., Mewaldt, R. A., Zhao, L., & Labrador, A. W. 2012, SSRv, 171, 141
Lin, R. P. 1985, SoPh, 100, 537
Lin, R. P., Anderson, K. A., Ashford, S., et al. 1995, SSRv, 71, 125
Lin, R. P., Mewaldt, R. A., & Van Hollebeke, M. A. I. 1982, ApJ, 253, 949
Mann, G. 2015, JPlPh, 81, 475810601
Masters, A., Stawarz, L., Fujimoto, M., et al. 2013, NatPh, 9, 164
Müller-Mellin, R., Böttcher, S., Falenski, J., et al. 2008, SSRv, 136, 363
Oka, M., Birn, J., Battaglia, M., et al. 2018, SSRv, 214, 82
Petrosian, V. 2016, ApJ, 830, 28
Reames, D. V. 1999, SSRv, 90, 413
Reames, D. V., von Rosenvinge, T. T., & Lin, R. P. 1985, ApJ, 292, 716
Richardson, I. G., von Rosenvinge, T. T., Cane, H. V., et al. 2014, SoPh, 289, 3059
Simnett, G. M., Sakai, J.-I., & Forsyth, R. J. 2005, A&A, 440, 759
Trotta, D., & Burgess, D. 2019, MNRAS, 482, 1154
Tsurutani, B. T., & Lin, R. P. 1985, JGR, 90, 1
von Rosenvinge, T. T., Reames, D. V., Baker, R., et al. 2008, SSRv, 136, 391
Wraase, S., Heber, B., Böttcher, S., et al. 2018, A&A, 611, A100
Xiong, M., Zheng, H., Wang, Y., & Wang, S. 2006, JGRA, 111, A11102
Yang, L., Wang, L., Li, G., et al. 2019, ApJ, 875, 104